Material characterization

1. Physical Characterization

The phase and crystal structure of the prepared catalyst material were determined by XRD powder diffractometer (PANalytical/Empyrean, Cu Kα radiation). The morphology and microstructure were characterized by a field emission scanning electron microscope (FESEM, FEI Tecnai G2 F30) and a transmission electron microscope (TEM, JEOL JEM-F200) equipped with an X-ray energy dispersive spectrometer. X-ray photoelectron spectroscopy (XPS) characterization is performed on a K-Alpha+ spectrometer equipped with a monochromatic aluminum X-ray light source to obtain the valence state distribution of the material. Raman spectroscopy (Raman) is obtained using Renishaw/INVIA REFLEX spectrometer.

2. Electrochemical characterization

2.1 Preparation of working electrode

Accurately weigh 5 mg of the sample and uniformly disperse it into a mixed solution containing 1 mL of ethanol, 0.5 mL of deionized water and 40 μL of 5 wt% Nafion under ultrasound at room temperature to make a catalyst ink. Subsequently, 150 μL of catalyst ink was dropped onto a 1×1 cm^2 carbon paper and dried at room temperature to be used as a working electrode. At this time, the catalyst loading was 0.48 mg cm^{-2}.

2.2 Electrochemical evaluations

CHI 760E electrochemical workstation (Shanghai Instruments Co., Ltd.) is used to record all electrochemical measurement results, and use a three-electrode system to evaluate the electrocatalytic activity of the prepared material for oxygen evolution reaction. Among them, Ag/AgCl (saturated KCl solution) and graphite rod electrode are used as reference electrode and counter electrode, respectively. The electrolyte solution uses 1.0 M KOH solution. The voltages used in the article are all relative to the reversible hydrogen electrode (RHE), using the following formula for conversion: $E_{RHE} = E_{Ag/AgCl} + 0.059 \times pH + 0.2017$. The overpotential is calculated by the difference between the voltage value corresponding to the polarization curve and the theoretical water splitting voltage, according to the following formula: $\eta = E_{RHE} - 1.23$ V. The polarization curve is obtained by linear sweep voltammetry (LSV) scanning at a rate of

5mV/s in the voltage range of 0.2-0.8 V vs. Ag/AgCl. The polarization curve is redrawn as η vs. log [current density (j)] to obtain the Tafel diagram, which is used to evaluate the OER kinetics of the catalyst. Fit the linear region in the Tafel diagram and combine the Tafel equation to obtain the Tafel slope ($\eta = b \log j + a$, where j represents the current density and b represents the Tafel slope). The LSV curve comparison before and after 2000 CV cycles was used to evaluate the OER stability of the material. The cycle interval of CV was 0.2-0.8 V vs. Ag/AgCl. In addition, the chronoamperometry (i-t) was further used to test the long-term stability of the catalyst at 1.6 V vs. RHE. The electrochemical double layer capacitance (Cdl) of the electrocatalyst was evaluated by using the CV test at different scanning speeds in the non-Faraday interval. The selected CV scan rate is 5, 10, 15, 20, 25 mV/s, and the measured potential range is 0.63-0.73 V vs. RHE. The value of C_{dl} is determined by the slope when $((j_a-j_c)/2)$ is plotted against the scan rate, where j_a and j_c represent the current density of the anode and cathode, respectively. All polarization curves are obtained with 80% iR compensation.

Turnover frequency (TOF) was calculated according to the following equation:

$$TOF=(J*A)/(4*F*n)$$

where J (mA cm^{-2}) is the current density at the specified overpotential, A (0.5 cm^2) is the area of the electrode, and F (96485 mol C^{-1}) is the Faraday constant, n is the total number of moles of active metal sites (Ni,Fe) deposited on the electrode (assuming all metals are involved in the reaction).

Faradaic efficiency analysis was performed on an RRDE. When a constant current (200 μA) was applied to the disk electrode to ensure the OER reaction to generate oxygen, and the ring potential was held constantly at 0.40 V vs. RHE to reduce the oxygen generated by the catalyst on the disk electrode. The Faraday efficiency FE can be calculated according to the following formula[1]:

$$FE=I_{ring}/(I_{disk}* N)$$

where I_{disk} denotes the disk current, I_{ring} denotes the ring current, and N denotes the current collection efficiency of the RRDE (0.43).

2.3 Calculation of electron transfer number (n) for the oxygen reduction reaction

The electron transfer number (n) can be calculated using the Koutecky-Levich (K-L) equation, the formula is as follows:

$$\frac{1}{J} = \frac{1}{B\omega^{1/2}} + \frac{1}{J_K} \quad (1)$$

$$B = 0.2nFC_0(D_0^{2/3})(v^{-\frac{1}{6}}) \quad (2)$$

$$J_K = nFKC_0 \quad (3)$$

In the above formula, J is the current density measured by RRDE, and J_k is the kinetic limiting current density. ω represents the angular velocity of the disc, calculated by ω = 2πN, where N is the linear rotation speed. Use n to represent the number of electrons transferred during the ORR reaction. F represents Faraday's constant (96485 $C \cdot mol^{-1}$). The volume concentration of O_2 is C_0, and the kinematic viscosity of the electrolyte is ν. k is the electron transfer rate constant, and D_0 is the diffusion coefficient of O_2 in the electrolyte. The speed is expressed in rpm, and 0.2 is taken as a constant. In this article, the electric potential and current density used to calculate the electron transfer number according to the K-L equation are the current density of the LSV curve at 0.40, 0.45 and 0.50 V, respectively, corresponding to each speed.

2.4 Zinc-air battery test

The electrocatalyst was uniformly dispersed on a 1×1 cm^2 gas diffusion layer to be used as the cathode of a zinc-air battery, with a load of 3.0 mg cm^{-2}. The polished zinc plate was used as the anode, and the 6.0 M KOH solution containing 0.2 M $Zn(Ac)_2$ was used as the electrolyte to assemble a water-based zinc-air battery and then evaluate its performance. Solid-state zinc-air batteries use polished zinc foil as the anode and gel polymer as the electrolyte. The electrolyte was prepared as follows: 0.8 g of polyvinyl alcohol (PVA) powder (M_w=30000~70,000) was added to 80 mL of deionized water and stirred at 95°C for 2 hours. Then 8 mL of 18.0 M KOH solution containing 0.2 M $Zn(Ac)_2$ was added, and the electrolyte solution was stirred at 95° C for 3 hours. The

electrolyte takes on a brownish yellow color. Then freeze the solution overnight, take it out before use and thaw it at room temperature to be used as an electrolyte. A mechanical mixture of commercial Pt/C and Ir/C (mass ratio 1:1) was used as a control. The battery was charged and discharged with a constant current for 20 minutes (10 minutes of charge and 10 minutes of discharge) at a current density of 5 mA cm^{-2} to evaluate the long-term charge-discharge cycle capability of water-based zinc-air batteries and solid-state zinc-air batteries. The constant current charge and discharge data are recorded by the LAND (CT2001A) battery test system.

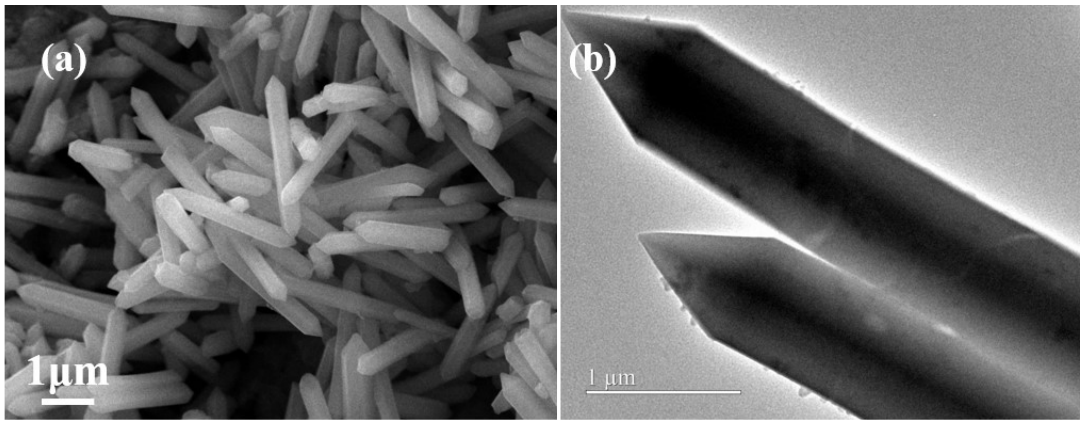

Figure S1. (a)SEM and (b)TEM images of the synthesized MIL-88A.

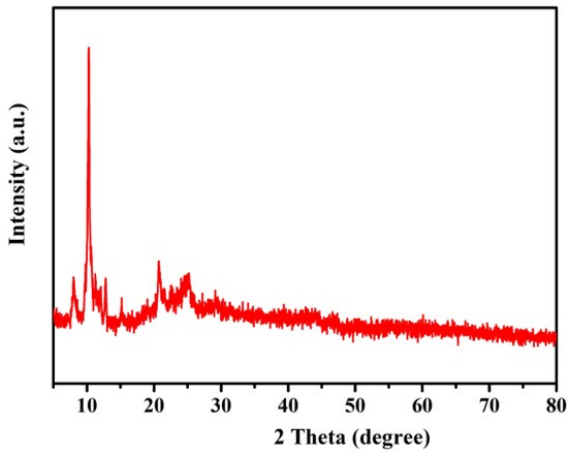

Figure S2. XRD diffraction pattern of the synthesized MIL-88A.

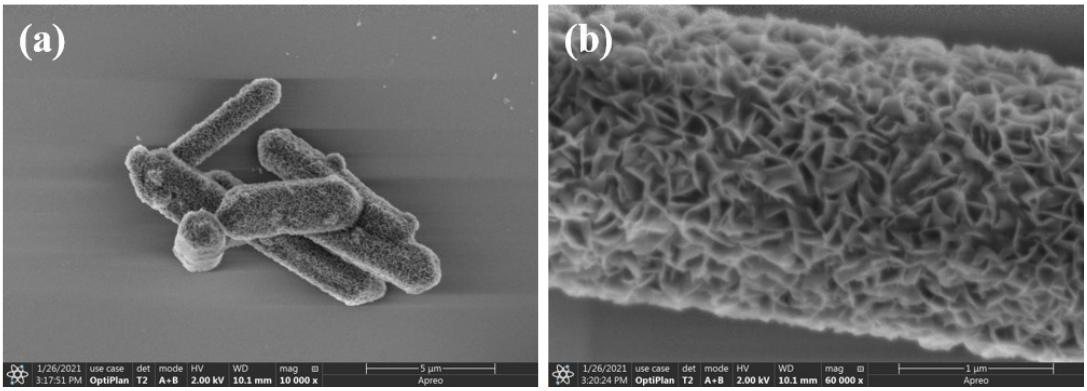

Figure S3. Morphology of the precursor MIL-88A/$Ni(OH)_2$ under different multiples, (a)×10000, (b)×60000.

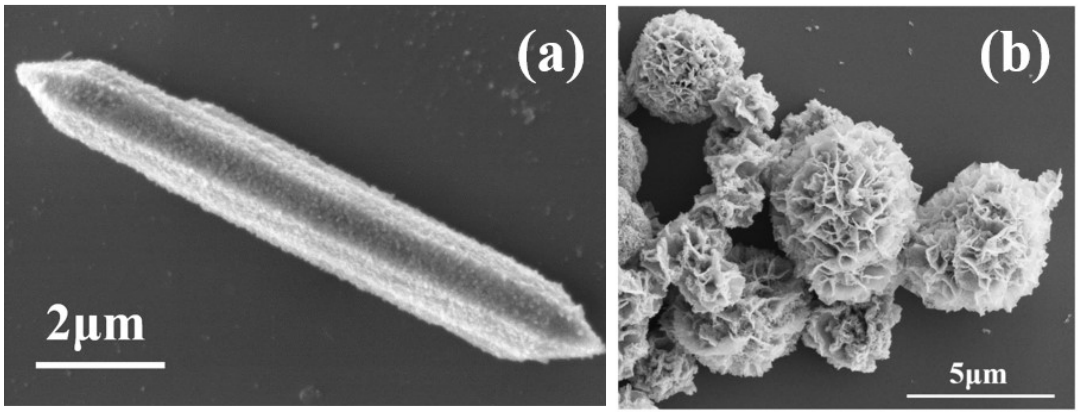

Figure S4. SEM images of (a) FeS_2 and (b)NiS_2 sample.

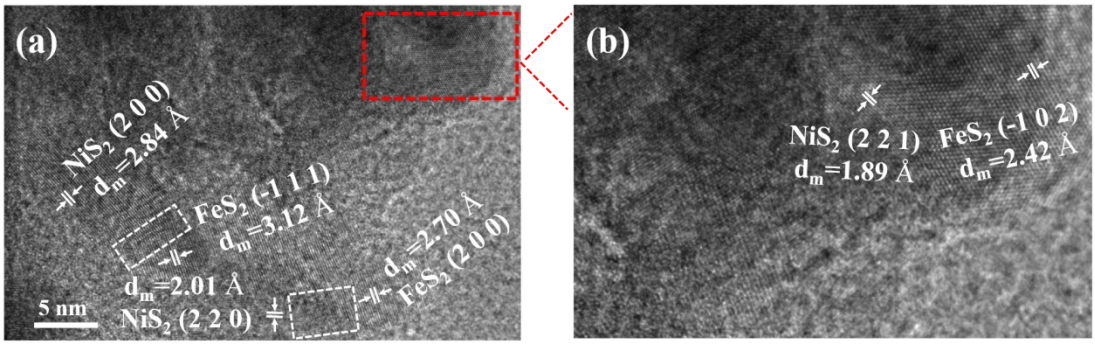

Figure S5. (a) HRTEM image of FeS_2/NiS_2 HDSNRs.(b) Magnified image of the selected lattice fringe.

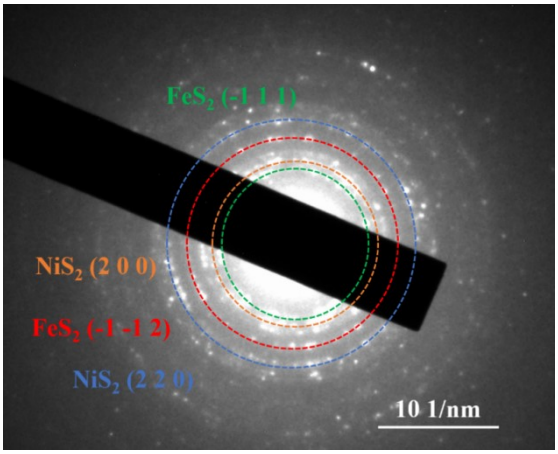

Figure S6. Selected area electron diffraction pattern of FeS_2/NiS_2 HDSNRs.

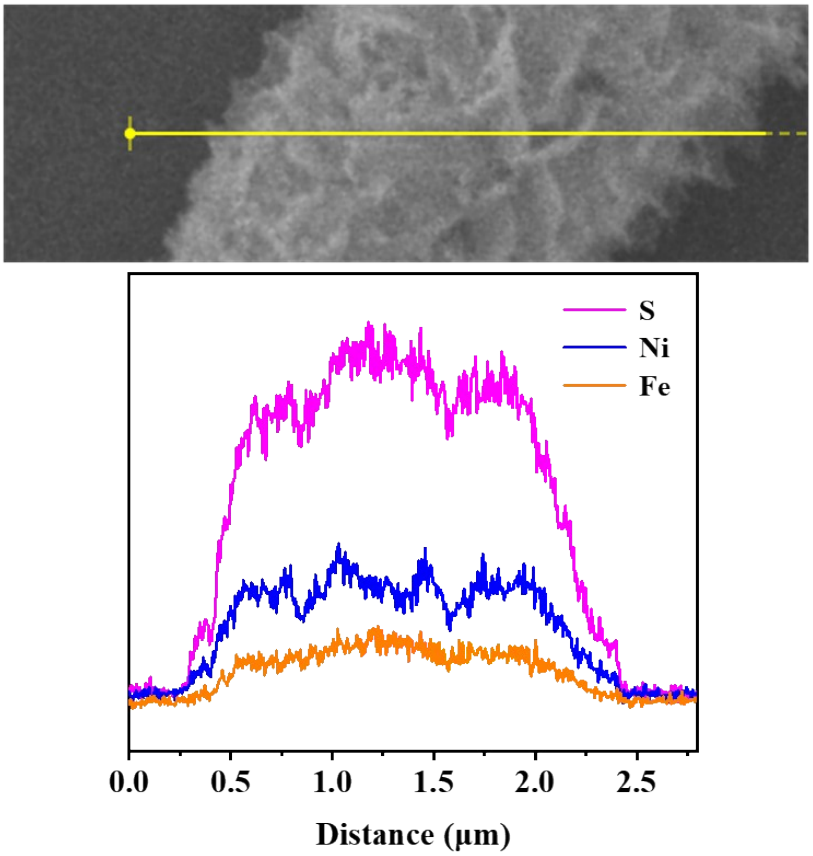

Figure S7. SEM image and the corresponding linear distributions.

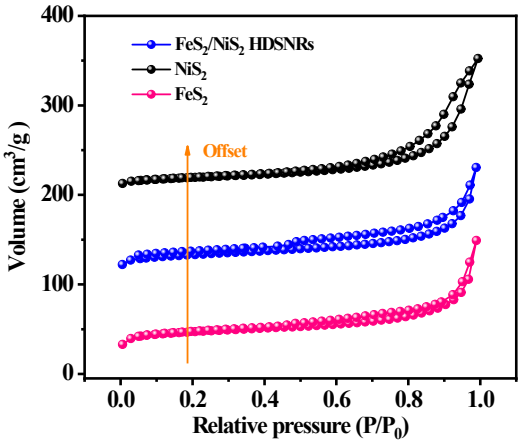

Figure S8. N_2 adsorption–desorption isotherms of FeS_2, NiS_2 and FeS_2/NiS_2 HDNRs.

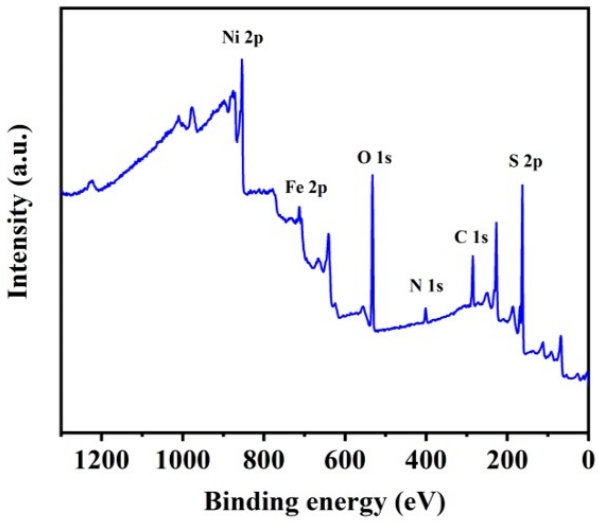

Figure S9. XPS survey spectrum of the synthesized sample FeS_2/NiS_2 HDSNRs.

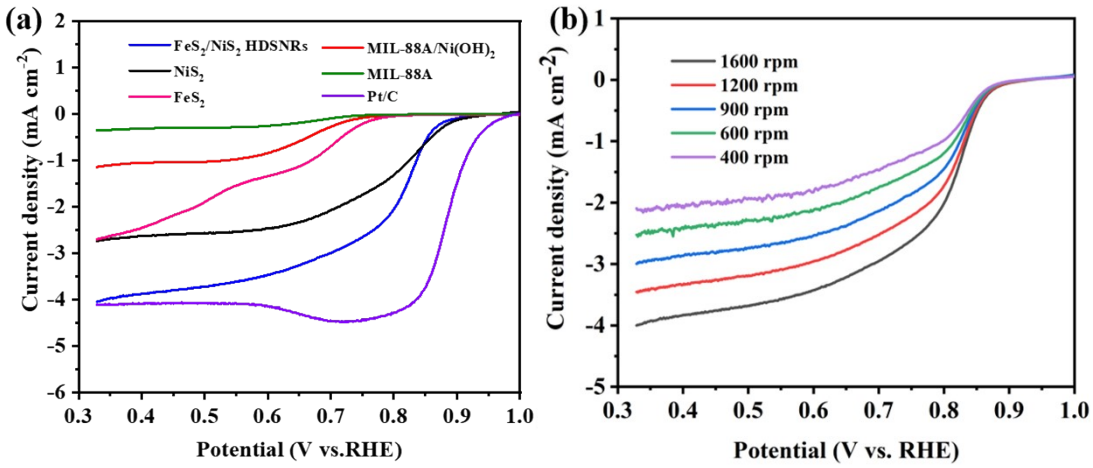

Figure S10. (a) LSV curves of Pt/C, FeS_2/NiS_2 HDSNRs, FeS_2 , MIL-88A, MIL-88A/$Ni(OH)_2$ and NiS_2 in O_2-saturaed 1.0 M KOH solution with a scan rates of 5 mV s^{-1} at 1600rpm. (b) LSV curve of FeS_2/NiS_2 HDSNRs at different speeds.

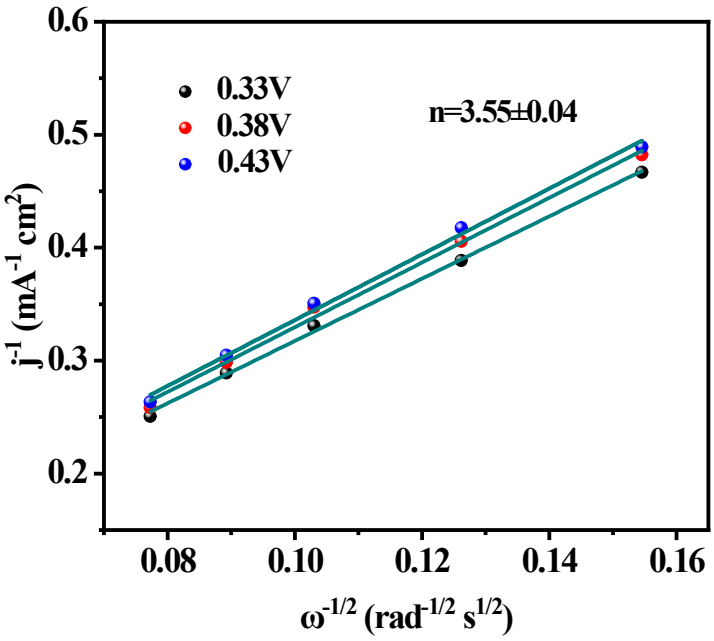

Figure S11. K–L plot of FeS_2/NiS_2 HDSNRs.

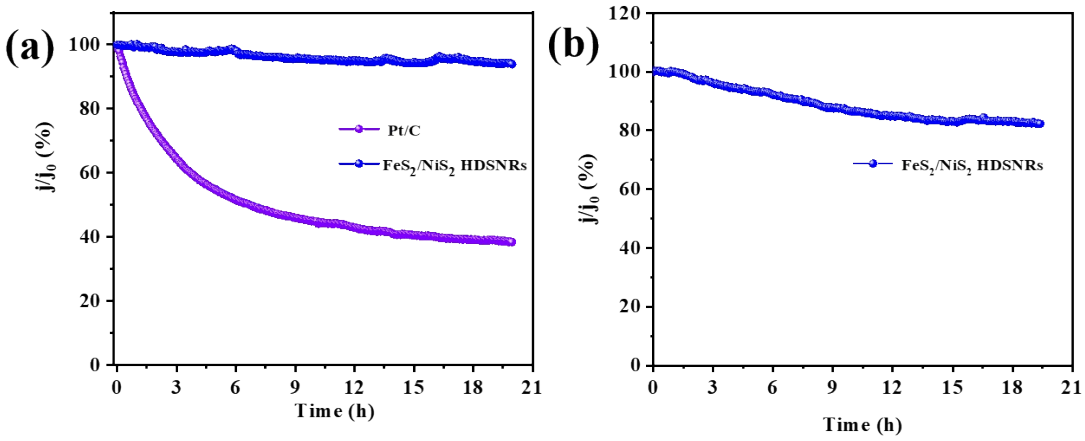

Figure S12. The i-t chronoampere response curves in O_2-saturated 1.0 M KOH solution: (a) FeS_2/NiS_2 HDSNRs and Pt/C at 0.80 V vs. RHE. (b) FeS_2/NiS_2 HDSNRs at 0.70 V vs. RHE.

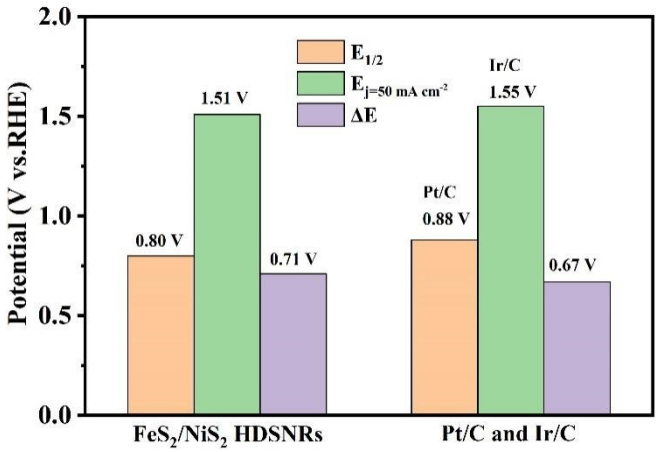

Figure S13. The histogram of the ORR and OER bifunctional activity ΔE of FeS_2/NiS_2 HDSNRs, Pt/C and Ir/C. (ΔE value is the difference between ORR half-wave potential and OER potential at a current density of 50 mA cm^{-2})

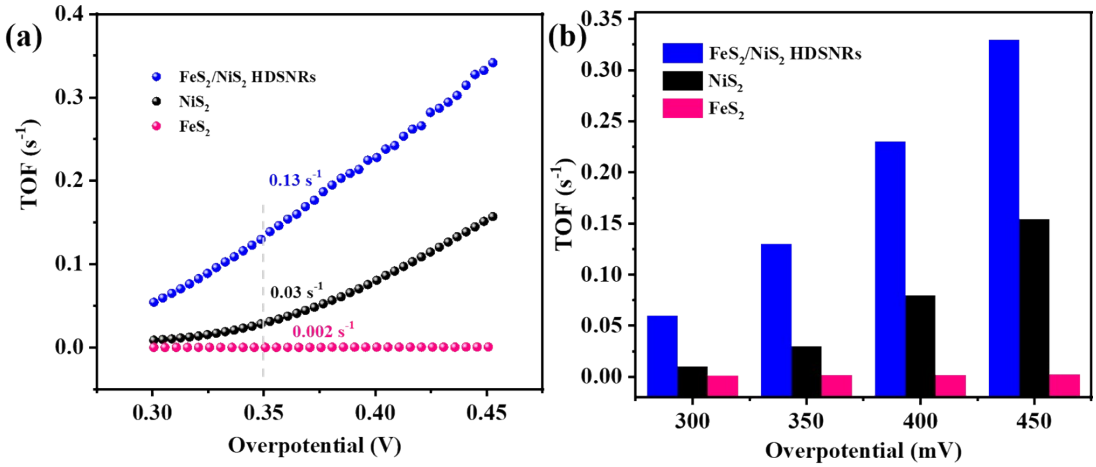

Figure S14. Figure (a) TOF curves of NiS_2, FeS_2 and FeS_2/NiS_2 HDSNRs catalysts at different overpotentials. (b) TOF values of each catalyst at overpotentials of 300, 350, 400, and 450 mV, respectively.

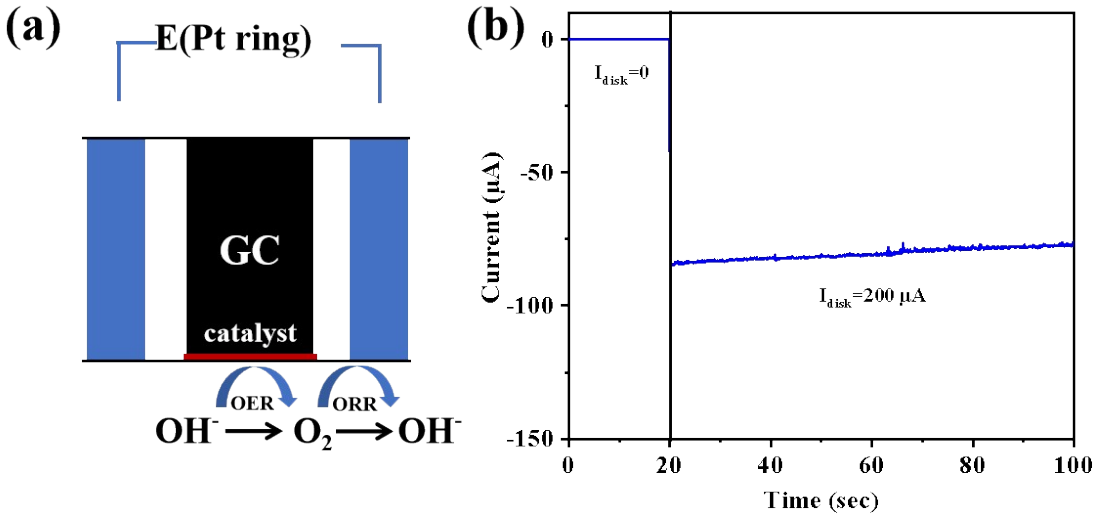

Figure S15. (a) Mechanism diagram of Faradaic efficiency testing with RRDE. (b) Ring current values detected when applying disk current of 200 μA, ring potential of 0.4 V vs. RHE. Testing for FeS_2/NiS_2 in N_2-saturated 1.0 M KOH solution.

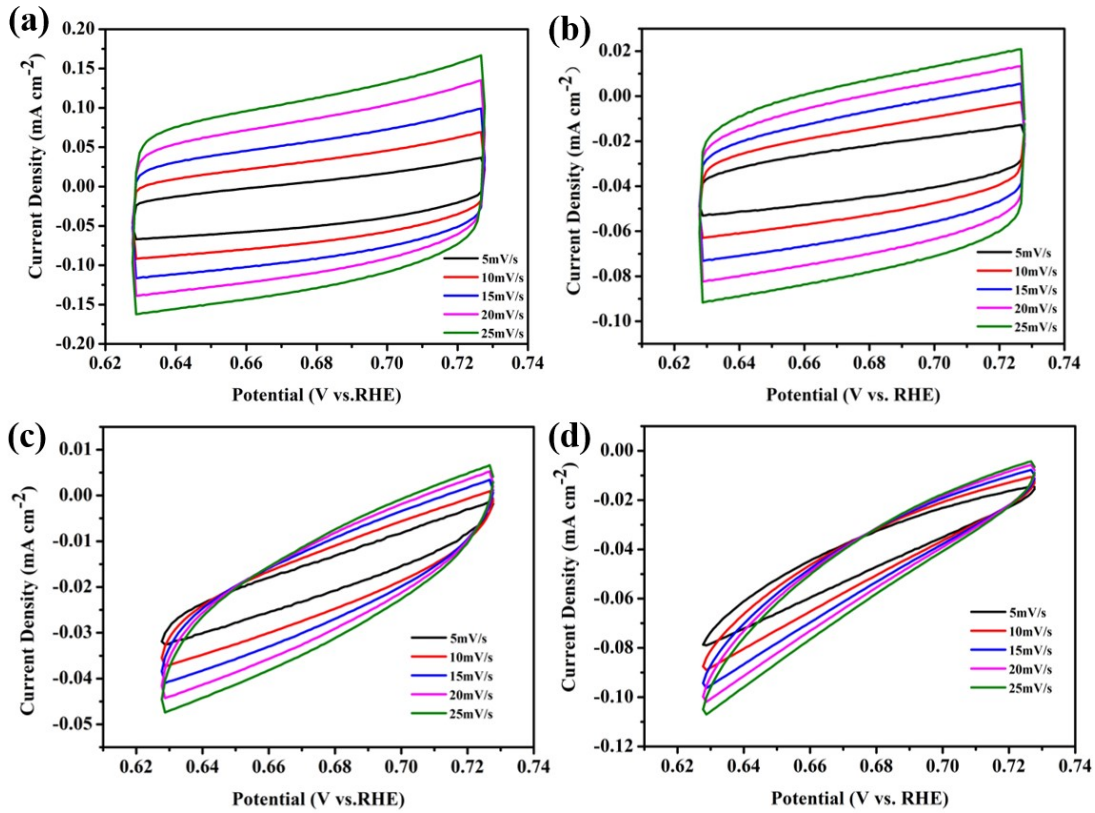

Figure S16. Cyclic voltammograms at different scanning speeds of (a) FeS_2/NiS_2 HDSNRs, (b) NiS_2, (c) FeS_2 and (d) MIL-88A/($Ni(OH)_2$) in the region of 0.63 V-0.73 V vs. RHE.

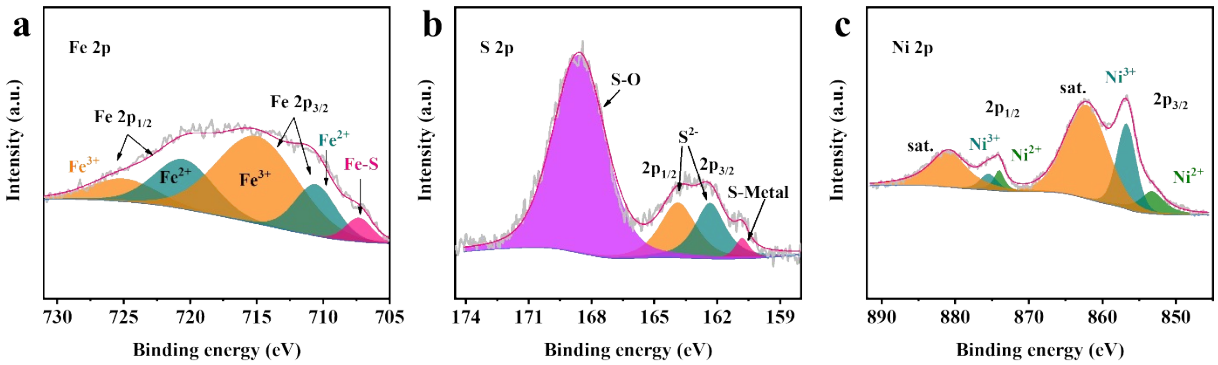

Figure S17. XPS spectra after long charge and discharge cycles: (a) Fe 2p; (b) S 2p; (c) Ni 2p.

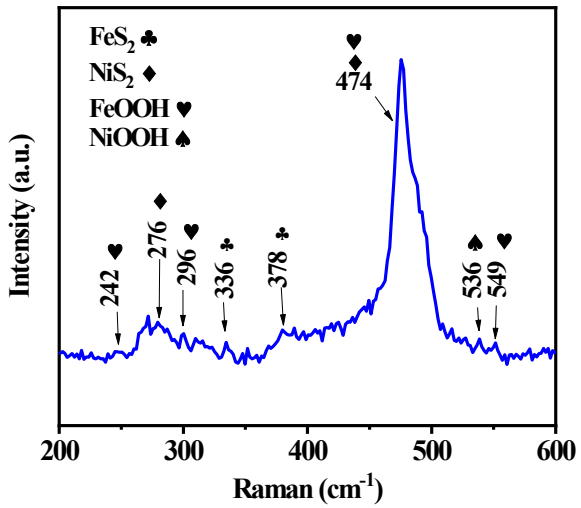

Figure S18. Raman spectrum after a long time charge and discharge cycle.

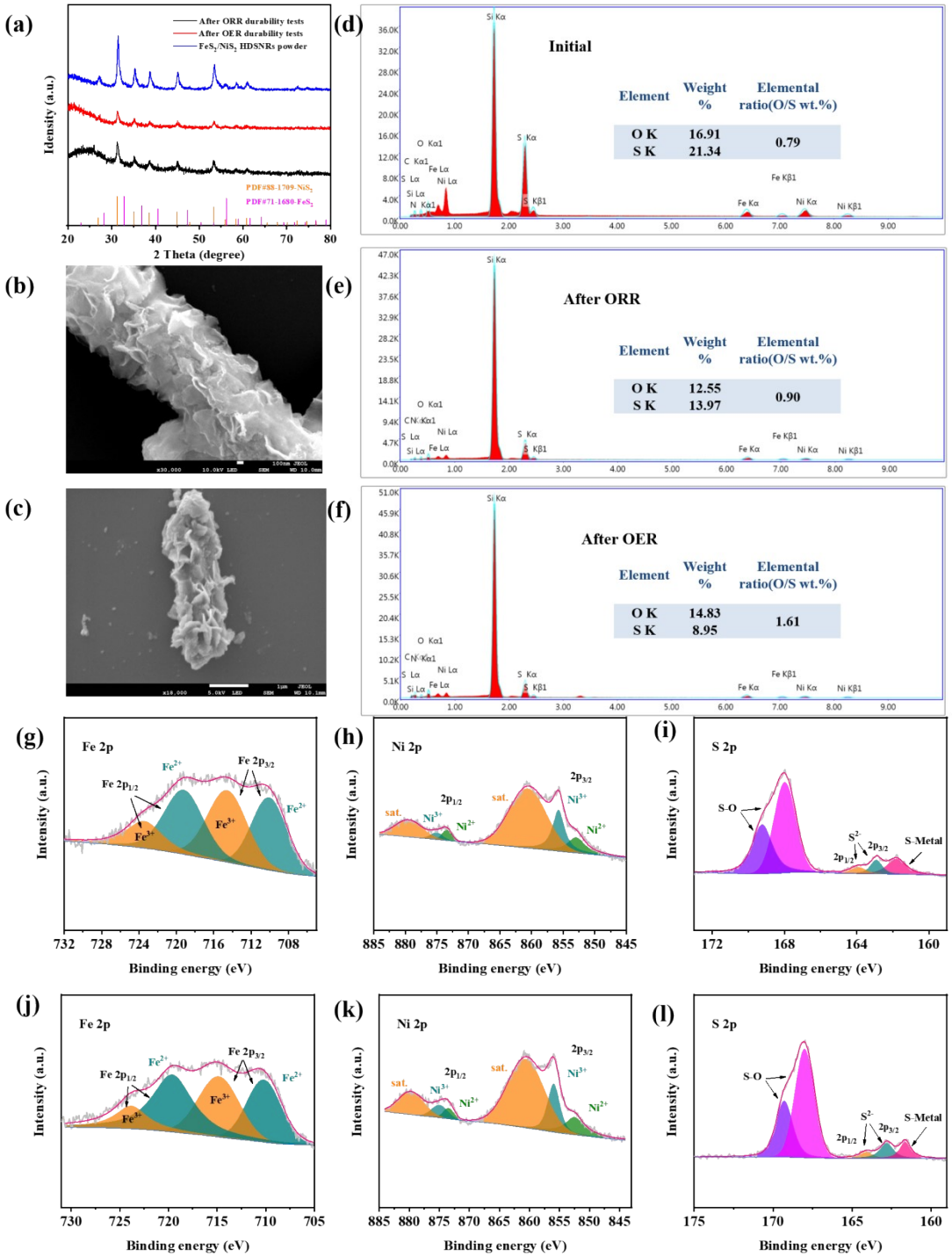

Figure S19. (a) XRD patterns of FeS_2/NiS_2 catalysts after ORR and OER durability tests. (b-c) SEM images of FeS_2/NiS_2 catalysts after ORR and OER durability tests, respectively. EDS spectra of (d) Initial, (e) After-ORR, and (f) After-OER FeS_2/NiS_2 electrodes. XPS spectra of FeS_2/NiS_2 catalysts after ORR durability test (g) Fe 2p, (h) Ni 2p and (i) S 2p. XPS spectra of catalysts after OER durability testing (j) Fe 2p, (k) Ni 2p and (l) S 2p.

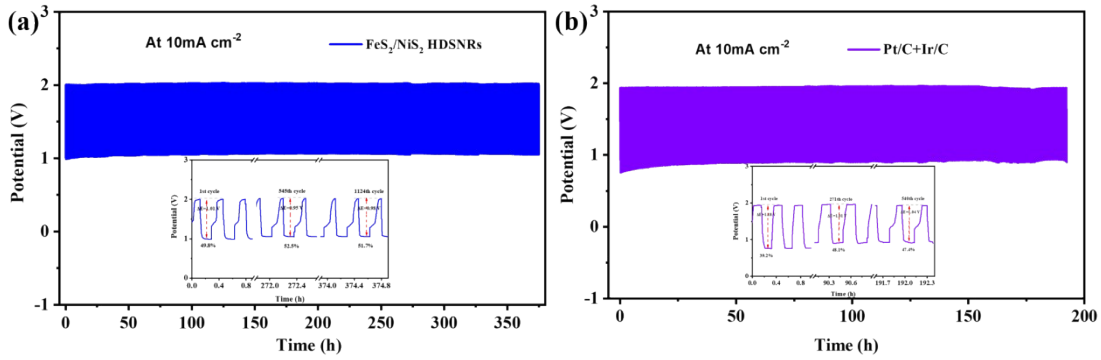

Figure S20. Charge/discharge curves of aqueous zinc-air batteries assembled with (a) FeS_2/NiS_2 HDSNRs and (b) Pt/C+Ir/C materials at 10 mA cm^{-2}. The corresponding the round-trip efficiency before and after galvanostatic cycling stability tests are shown in the inset.

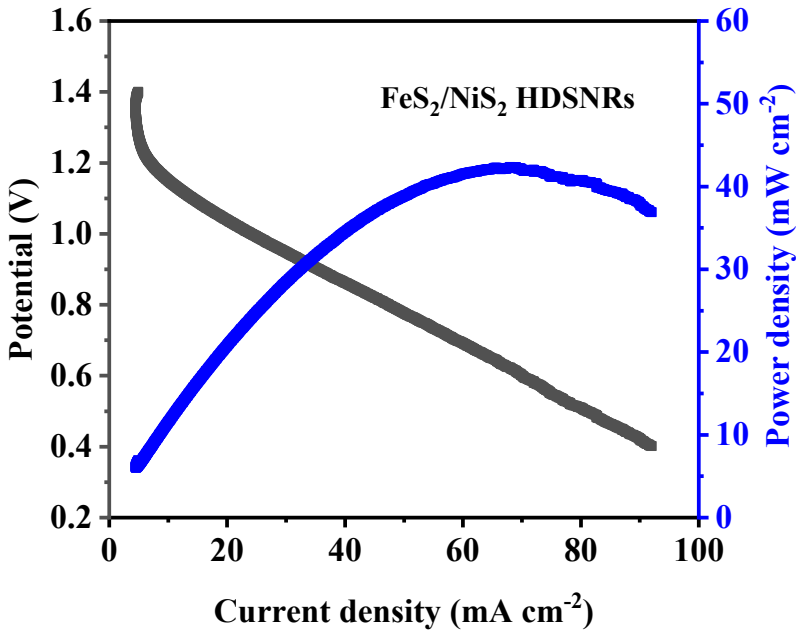

Figure S21. Discharge polarization curve and peak power density curve of FeS_2/NiS_2 HDSNRs catalysts as the cathode of a solid state zinc-air battery.

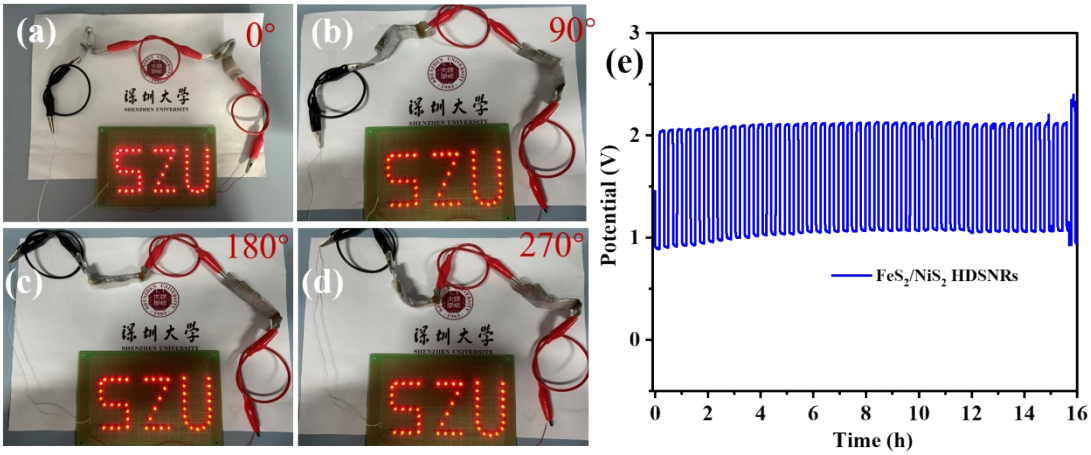

Figure S22. (a-d) Digital photos of the assembled flexible solid-state batteries lighting LEDs at different bending angles (0°, 90°, 180°, 270°). (e) Charge/discharge cycle curves of the solid-state battery tested at 90° bending angle.

Table S1. Comparison of catalyst performance reported in the literature

Electrocatalysts	η_{OER} (mV) at 10 mV cm^{-2}	$Tafel_{OER}$ (mV dec^{-1})	Onset potential (E_{onset} vs.RHE)	Half potential ($E_{1/2}$ vs.RHE)	References
FeS_2/NiS_2	**280(@50m A cm^{-2})**	**33.0**	**0.88**	**0.80**	**This work**
NiS_2/CoS_2	295	51.0	0.90	0.79	[2]
(Ni, Fe)S_2 @MoS_2	270	43.2	/	/	[3]
Fe-$NiCo_2O_4$	302	42.0	/	/	[4]
(Ni,Co)S_2	270	58.0	0.82	0.71	[5]
Ni_3S_2/NF	260	/	/	/	[6]
MIL-88A/$Ni(OH)_2$-CC	300(@30m A cm^{-2})	36.4	/	/	[7]
$NiCo_2S_4$@NiFe LDH	287	86.4	0.97	0.85	[8]
$MnFe_2O_4$ /$NiCo_2O_4$	344	46.7	0.88	0.767	[9]
O-NiCoFe-LDH	300	93.0	0.80	0.63	[10]
FeNi nanoparticles encapsulated in NCNTs	290	37.0	0.93	0.81	[11]
N_2-NiS_2-500	270	/	/	/	[12]

Table S2. Table The ICP results of NiS_2, FeS_2 and FeS_2/NiS_2 HDSNRs.

Sample	Fe (wt.%)	Ni (wt.%)
FeS_2/NiS_2 HDSNRs	**5.59**	**34.86**
NiS_2	**-**	**40.03**
FeS_2	**25.60**	**-**

Table S3. Comparison of the stability of NiFe composites reported in the literature for zinc-air batteries

Cathode catalysts	Stability	References
FeS_2/NiS_2 HDSNRs	480 h at 5 mA cm^{-2} 380 h at 10 mA cm^{-2}	This work
$(Ni,Co)S_2$	480 h at 2 mA cm^{-2}	5
NiS_2	＞40 h at 10 mA cm^{-2}	13
$NiFe_2O_4/Ni_3S_4$	70 h at 10 mA cm^{-2}	14
NiS_x/NMC-1.5	100 h at 10 mA cm^{-2}	15
NiS_x/S-rGO	200 h at 15 mA cm^{-2}	16
FeS_2/NiS_2 hybrid nanocrystals	25 h at 3 mA cm^{-2}	17

References

1. S. Zhao, Y. Wang, J. Dong, C.-T. He, H. Yin, P. An, K. Zhao, X. Zhang, C. Gao and L. Zhang, *Nature Energy*, 2016, **1**, 1-10.

2. Y. Cao, X. Zheng, H. Zhang, J. Zhang, X. Han, C. Zhong, W. Hu and Y. Deng, *Journal of Power Sources*, 2019, **437**, 226893.

3. Y. Liu, S. Jiang, S. Li, L. Zhou, Z. Li, J. Li and M. Shao, *Applied Catalysis B: Environmental*, 2019, **247**, 107-114.

4. F. Lai, J. Feng, X. Ye, W. Zong, G. He, Y.-E. Miao, X. Han, X. Y. Ling, I. P. Parkin, B. Pan, Y. Sun and T. Liu, *Journal of Materials Chemistry A*, 2019, **7**, 827-833.

5. J. Zhang, X. Bai, T. Wang, W. Xiao, P. Xi, J. Wang, D. Gao and J. Wang, *Nano-micro letters*, 2019, **11**, 1-13.

6. L.-L. Feng, G. Yu, Y. Wu, G.-D. Li, H. Li, Y. Sun, T. Asefa, W. Chen and X. Zou, *Journal of the American Chemical Society*, 2015, **137**, 14023-14026.

7. Z. Qian, K. Wang, K. Shi, Z. Fu, Z. Mai, X. Wang, Z. Tang and Y. Tian, *Journal of Materials Chemistry A*, 2020, **8**, 3311-3321.

8. X. Feng, Q. Jiao, W. Chen, Y. Dang, Z. Dai, S. L. Suib, J. Zhang, Y. Zhao, H. Li and C. Feng, *Applied Catalysis B: Environmental*, 2021, **286**, 119869.

9. Y.-Q. Zhang, M. Li, B. Hua, Y. Wang, Y.-F. Sun and J.-L. Luo, *Applied Catalysis B: Environmental*, 2018, **236**, 413-419.

10. L. Qian, Z. Lu, T. Xu, X. Wu, Y. Tian, Y. Li, Z. Huo, X. Sun and X. Duan, *Advanced Energy Materials*, 2015, **5**, 1500245.

11. R. Nandan, A. Gautam and K. K. Nanda, *Journal of Materials Chemistry A*, 2018, **6**, 20411-20420.

12. J. Hao, W. Yang, J. Hou, B. Mao, Z. Huang and W. Shi, *Journal of Materials Chemistry A*, 2017, **5**, 17811-17816.

13. X. Shi, X. Ling, L. Li, C. Zhong, Y. Deng, X. Han and W. Hu, *Journal of Materials Chemistry A*, 2019, **7**, 23787-23793.

14. Z. Fu, S. Liu, Z. Mai, Z. Tang, D.-D. Qin, Y. Tian and X. Wang, *Chemistry-An Asian Journal*, 2020, **15**, 3568-3574.

15. K. Wan, J. Luo, X. Zhang, C. Zhou, J. W. Seo, P. Subramanian, J.-W. Yan and J. Fransaer, *Journal of Materials Chemistry A*, 2019, **7**, 19889-19897.

16. A. Sumboja, J. Chen, Y. Ma, Y. Xu, Y. Zong, P. S. Lee and Z. Liu, *Chemcatchem*, 2019, **11**, 1205-1213.

17. J. Jin, J. Yin, H. Liu and P. Xi, *Chinese Journal of Catalysis*, 2019, **40**, 43-51.